An image-focusing semblance functional for velocity analysis

Biondo Biondi

ABSTRACT

Analyzing the focusing and defocusing of migrated images provides valuable velocity information that can supplement the velocity information routinely extracted from migrated common-image gathers. However, whereas qualitative focusing analysis is readily performed on ensemble of images generated by prestack residual migration, quantitative focusing analysis remains a challenge. I use two simple synthetic-data examples to show that the maximization of a minimum-entropy norm, a commonly-used measure of image focusing, yields accurate estimates for diffracted events, but it can be misleading in the presence of continuous but curved reflectors.

I propose to measure image focusing by computing coherency across structural dips, in addition to coherency across aperture/azimuth angles. Images can be efficiently decomposed according to structural dips during residual migration. I introduce a semblance functional to measure image coherency simultaneously across the aperture/azimuth angles and the dip angles. Using 2D synthetic data examples, I show that the simultaneous evaluation of semblance across aperture-angles and dips can be effective in quantitatively measuring image focusing and also avoiding the biases induced by reflectors' curvature.

INTRODUCTION

Even a superficial analysis of depth migrated seismic images obtained with different migration velocities clearly shows that velocity information could be extracted by measuring image focusing along the spatial dimensions (i.e. horizontal axes and depth). This information is particularly abundant in areas where complex structure and discontinuous reflectors reveal lack of focusing caused by velocity errors; such as in presence of faults, point diffractors, buried channels, uncomformities or rough salt/sediment interfaces.

If we were able to extract this focusing-velocity information reliably from migrated images it could supplement the velocity information that we routinely extract by analyzing residual moveout along the offsets or aperture-angles axes, and thus enhance velocity estimation by increasing resolution and decrease uncertainties. It would be particularly useful to improve the interpretability of the final image and the accuracy of time-to-depth conversion in areas where the reflection aperture range is narrow

either because of unfavorable depth/offset ratio or because of the presence of fast body in the overburden (e.g. salt bodies) that deflect the propagating waves. Today, the most common application of image focusing is to migration-velocity scans for subsalt imaging (Wang et al., 2006). However, current practical applications exploit the image-focusing information by using subjective interpretation criteria instead of quantitative measurements (Sava et al., 2005). This limitation makes almost impossible to automate the process and potentially reduces its reliability, and thus it is a serious obstacle to its extensive application.

Minimum entropy has been often proposed as a quantitative measure of image focusing, starting with Harlan et al. (1984), De Vries and Berkhout (1984), and more recently by Stinson et al. (2005) and Fomel et al. (2007). Minimizing the "spatial entropy" measured on image windows privileges images that consist of isolated spikes. If the reflectivity function consists of isolated diffractors, minimum entropy is a good indicator of image focusing. However, field data are usually a combination of diffracted events, specular reflections from planar reflectors, and reflections for high-curvature reflectors. In these cases minimum entropy may yield bias estimates unless the diffractions are successfully separated from the other events before performing the analysis (Fomel et al., 2007). In complex geology, this separation can be unreliable when performed in the data space, and even more challenging when performed in the image space because it is biased by the initial migration velocity. In the following section I show that in presence of reflector curvature (e.g. a sinusoidal reflector) measuring focusing by minimum entropy leads to under-migrated images of convex reflectors (e.g. an anticline,) and over-migrated images of concave reflectors (e.g. a syncline.)

I aim to overcome these shortcomings by generalizing the conventional concept of semblance commonly used in velocity analysis. In addition to measuring semblance along the reflection-aperture angle (or offset for Kirchhoff migration,) as is routinely done, I propose to measure semblance along the structural-dip axes. In this paper I work with 2D data, and thus I compute semblance on 2D patches (structural dip and aperture angle.) With 3D full-azimuth data, semblance would be computed on 4D patches (indexed by two structural dips, reflection aperture and reflection azimuth.)

The proposed method can be applied to locally select the best-focused image among an ensemble of images obtained with different migration velocities. I use residual prestack depth migration in the angle domain (Biondi, 2008) to generate this ensemble of images starting from prestack depth-migrated image in the angle domain. Stolt prestack depth migration could be used as well to perform residual prestack migration (Sava, 2003). With either choice of residual migration, the image decomposition according to structural dip is easily performed within the residual prestack migration process, since both migrations require the image to be transformed into the spatial Fourier domain. The final goal, not addressed by this paper, is to use the image focusing information to enhance interval-velocity estimation for depth migration. In particular, I plan to update the interval-velocity model by using the wave-equation migration velocity analysis method starting from a spatially-varying field of

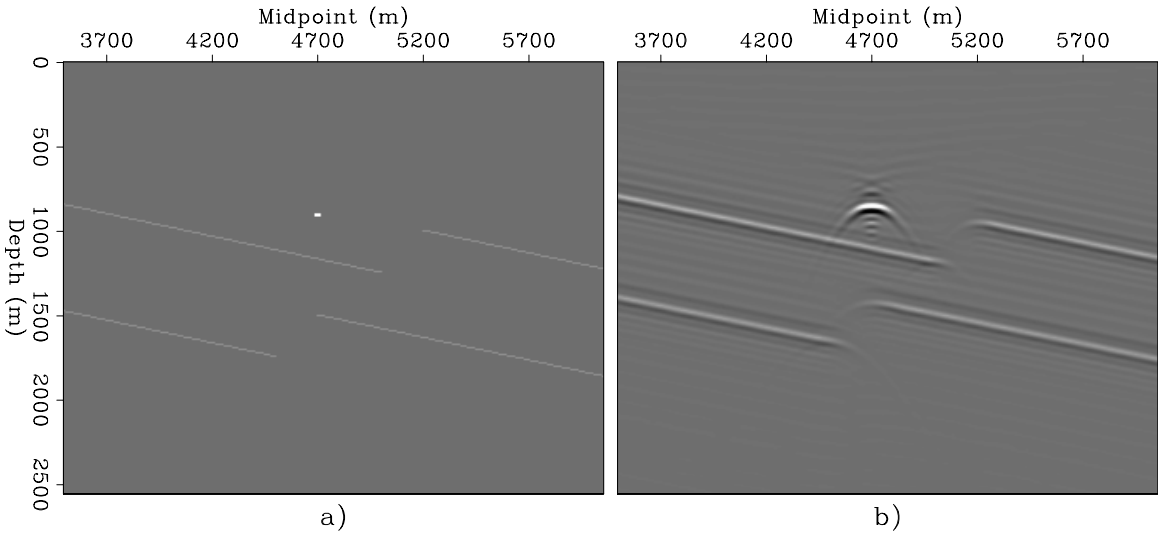

Figure 1: (a) Reflectivity function assumed to compute a synthetic prestack data set, and (b) the stacked section obtained by migrating the data set with a low velocity. [**CR**]

optimal-focusing parameters (Biondi and Sava, 1999; Sava and Biondi, 2004a,b; Sava, 2004).

THE CHALLENGE OF QUANTIFYING IMAGE FOCUSING

In this section, I introduce two simple synthetic data sets that illustrate the opportunities and challenges of measuring image focusing for velocity analysis. I start by showing how the application of a minimum entropy functional can help to determine the correct migration velocity, but also it can mislead the estimation.

Figure 1a and Figure 2a show the reflectivity functions assumed to generate the two data sets. The first one contains a strong diffractor and two dipping planar reflectors broken by a fault. Focusing analysis of the diffractor and the reflectors' truncations provides velocity information additional to the one available by conventional analysis of the reflections from the planar interfaces. The second model consists of a continuous sinusoidal reflector. It shows the potential pitfalls of measuring image focusing in presence of curvature in the structure. Figure 1b and Figure 2b show the result of migrating with a low velocity the modeled data corresponding to the reflectivity functions shown in Figure 1a and Figure 2a, respectively. In Figure 1b both the image of the point diffractor and the image of the reflectors' truncations show the typical signs of undermigration; that is, not fully collapsed diffracted events. In Figure 2b the bottom of the syncline shows triplication that are signs of undermigration, whereas the top of the anticline does not show any clear defocusing problems.

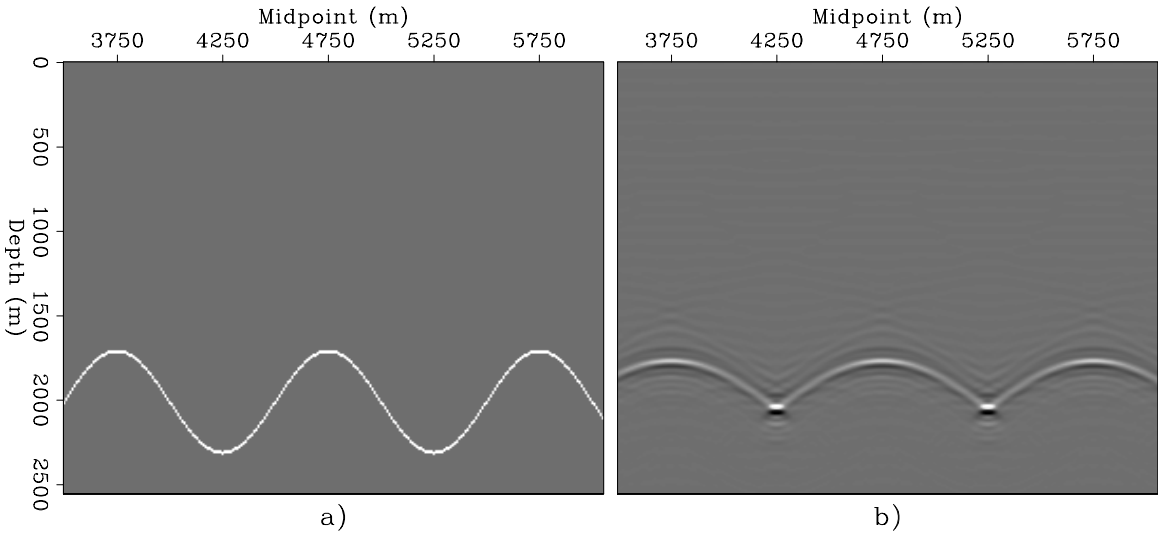

Figure 2: (a) Reflectivity function assumed to compute a synthetic prestack data set, and (b) the stacked section obtained by migrating the data set with a low velocity. [**CR**]

Pitfalls of Minimum Entropy functional

Minimizing the image entropy measured on moving spatial windows is a well-known approach to measuring image focusing. The varimax norm (Wiggins, 1985) is commonly used to measure the "entropy" of an image instead of the conventional entropy functional. The varimax norm is cheaper to evaluate than the conventional entropy functional because it does not require the evaluation of a logarithmic function. A peak in the varimax corresponds to a point of minimum entropy. I computed the varimax for local windows extracted from image ensembles computed by applying residual prestack migration to an initial prestack migration performed with a low velocity.

I define $\mathbf{R}\left(\mathbf{x},\gamma,\rho\right)$ as an ensemble of prestack images obtained by residual prestack migration where the parameter ρ is the ratio between the new migration velocity and the migration velocity used for the initial migration. The aperture angle is γ and $\mathbf{x}=\{z,x\}$ is the vector of spatial coordinates, where z is depth and x is the horizontal location.

I define the image window $\bar{\mathbf{x}}$ as:

$$\bar{\mathbf{x}}:\left\{\bar{z}-\Delta z\leq z\leq\bar{z}+\Delta z,\bar{x}-\Delta x\leq x\leq\bar{x}+\Delta x\right\}, \tag{1}$$

where $2\Delta z$ is the height of the window and $2\Delta x$ is its width, and $\bar{z}$ and $\bar{x}$ are the coordinates of the window's center.

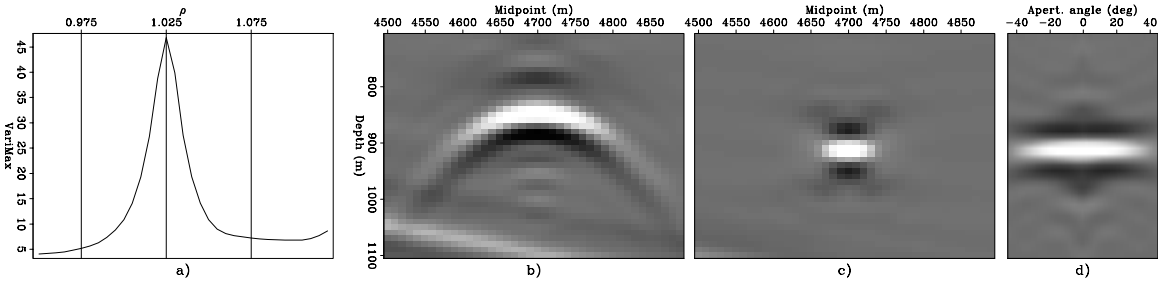

Figure 3: (a) Graph of the varimax norm as a function of ρ, (b) stacked section for $\rho = 1$, (c) stacked section for $\rho = 1.025$, and (d) angle-domain common image gather for $\rho = 1.025$ at $x = 4,700$ meters. [**CR**]

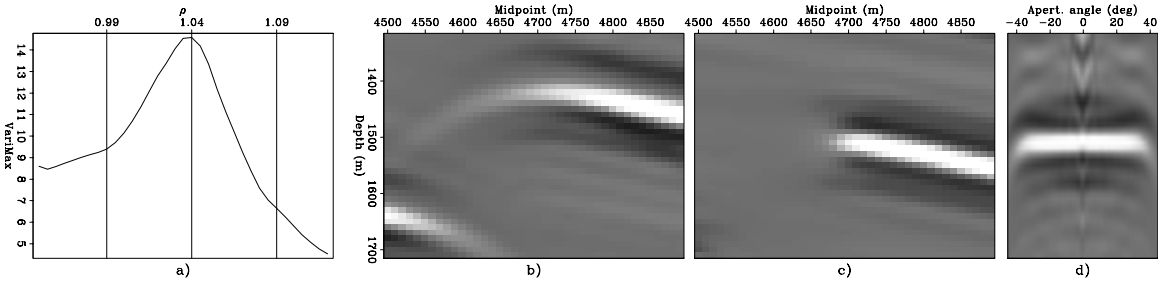

Figure 4: (a) Graph of the varimax norm as a function of ρ, (b) stacked section for $\rho = 1$, (c) stacked section for $\rho = 1.04$, and (d) angle-domain common image gather for $\rho = 1.04$ at $x = 4,700$ meters. [**CR**]

The varimax norm computed for $\bar{\mathbf{x}}$ is defined as:

$$E_{\mathbf{x}}(\rho) = \frac{N_{\bar{\mathbf{x}}} \sum_{\bar{\mathbf{x}}} \left[\sum_{\gamma} \mathbf{R}(\mathbf{x}, \gamma, \rho) \right]^4}{\left\{ \sum_{\bar{\mathbf{x}}} \left[\sum_{\gamma} \mathbf{R}(\mathbf{x}, \gamma, \rho) \right]^2 \right\}^2}, \tag{2}$$

where $\sum_{\mathbf{x}}$ signifies summation over all the image points in $\bar{\mathbf{x}}$ and $N_{\bar{\mathbf{x}}}$ is the number of points in $\bar{\mathbf{x}}$. Notice that the varimax in equation 2 includes stacking over the aperture angle γ.

For the first data set (Figure 1,) I computed the varimax in equation 2 as a function of ρ in two windows: the first centered on the point diffractor, the second centered on the reflector truncation. Figure 3 shows the following four plots for the point-diffractor window: a) the graph of the varimax norm as a function of ρ, b) the stacked section for $\rho = 1$; that is, the window of the initial undermigrated section in Figure 1b, c) the stacked section for $\rho = 1.025$; that is; for the peak of the curve shown in Figure 3a, and d) the angle-domain common image gather for the same value of $\rho = 1.025$ and extracted from the prestack cube at the horizontal location of the point diffractor.

Figure 4 shows analogous plots as the ones shown in the previous figure, but

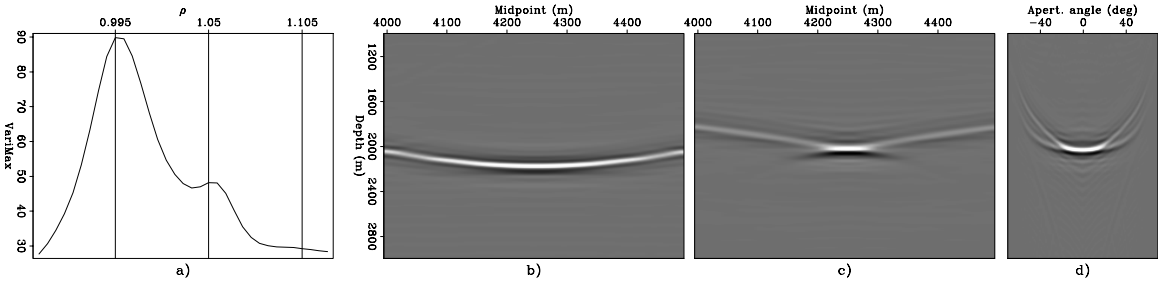

Figure 5: (a) Graph of the varimax norm as a function of ρ, (b) stacked section for $\rho = 1.06$, (c) stacked section for $\rho = .995$, and (d) angle-domain common image gather for $\rho = .995$ at $x = 4,250$ meters. [**CR**]

for the reflector-truncation window. Figure 4a shows the graph of the varimax as a function of ρ. Figure 4b shows the stacked section for $\rho = 1$. Figure 4c shows the stacked section for $\rho = 1.04$; that is, for the peak of the curve shown in Figure 4a, whereas Figure 4d shows the angle-domain common image gather for the same value of $\rho = 1.04$ and extracted from the prestack cube at the horizontal location of the reflector's truncation.

For both windows, the maximum of the varimax norm corresponds to the value of ρ that best focuses the prestack image and best flattens the angle-domain common image gathers. The semblance peak for the point diffractor is sharper than for the reflector truncation, suggesting that point diffractors provide higher-resolution information on migration velocity than reflectors' truncations.

I also computed the varimax in equation 2 as a function of ρ in two windows of the prestack migrated image corresponding to the sinusoidal reflector (Figure 2.) The first window is centered on the bottom of the syncline and the second centered on the top of the anticline. Figure 5 and Figure 6 show: a) graphs of the varimax as function of ρ, b) the stacked sections corresponding the correct values of ρ ($\rho = 1.06$ for Figure 5b and $\rho = 1.045$ for Figure 6b,) c) the stacked sections corresponding the the varimax peaks ($\rho = .995$ for Figure 5c and $\rho = 1.105$ for Figure 6c,) and d) the angle-domain common image gathers extracted at the very bottom of the syncline in Figure 5d and top of the anticline in Figure 6d.

For the first window, the peak of the varimax corresponds to a value of ρ that is too low, whereas for the second window the peak of the varimax corresponds to a value of ρ that is too high. The cause of these errors is that the image of concave reflectors can be made more spiky (i.e. lower entropy) by undermigration than by migration with the correct velocity. Similarly, the image of a convex reflector can be made more spiky by overmigration than by migration with the correct velocity. If the varimax norm were used to determine the residual-migration parameter ρ it would lead to images with wrong structure and non-flat common-image gathers. However, the secondary peaks of the varimax norm in both Figure 5 and Figure 6 are approximately located at the correct value of ρ. This secondary peaks indicate that there is potentially

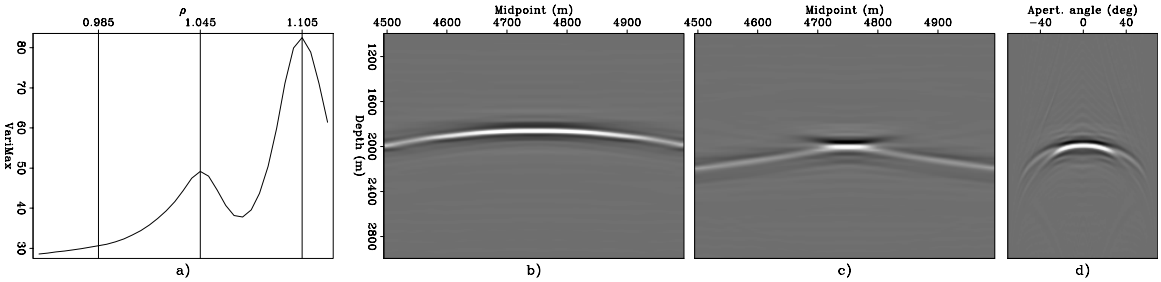

Figure 6: (a) Graph of the varimax norm as a function of ρ, (b) stacked section for $\rho = 1.045$, (c) stacked section for $\rho = 1.105$, and (d) angle-domain common image gather for $\rho = 1.105$ at $x = 4,750$ meters. [**CR**]

useful focusing information in the images, but to be practically useful we must devise a method that is not biased by the reflectors' curvature.

Measuring image coherency across structural dips

As an alternative to minimizing entropy, in this paper I propose to measure image focusing by maximizing coherency along both the structural-dip axes and the aperture/azimuth axes. The simultaneous use of dips and aperture angles is discussed in the next section. In this section, I show that measuring coherency along the structural dips does provide information on image focusing and I illustrate the concept by using the same two 2D synthetic data sets shown above. I will also demonstrate that maximizing coherency only along the structural dips may lead us to similar problems as the minimization of entropy.

To measure coherency along the structural dip α, I first create the dip-decomposed prestack image $\mathbf{R}(\mathbf{x}, \gamma, \alpha, \rho)$ by residual prestack migration, and then I compute the following semblance functional:

$$S_\alpha(\mathbf{x}, \rho) = \frac{\left[\sum_\alpha \sum_\gamma \mathbf{R}(\mathbf{x}, \gamma, \alpha, \rho)\right]^2}{N_\alpha \sum_\alpha \left[\sum_\gamma \mathbf{R}(\mathbf{x}, \gamma, \alpha, \rho)\right]^2}, \tag{3}$$

where N_α is the number of dips to be included in the computation. Notice that, as for the varimax in equation 2, semblance along structural dips is computed after stacking over the aperture angle γ.

The determination of the dip summation range at each image location and for each value of the parameter ρ is a practical problem of the proposed method. For the examples shown in this paper I determined the summation ranges for both α and γ by applying an amplitude thresholding criterion based on both local and global amplitude maxima measured from the images. To improve the smoothness of the semblance spectra, I averaged the evaluation of equation 3, and of all the other

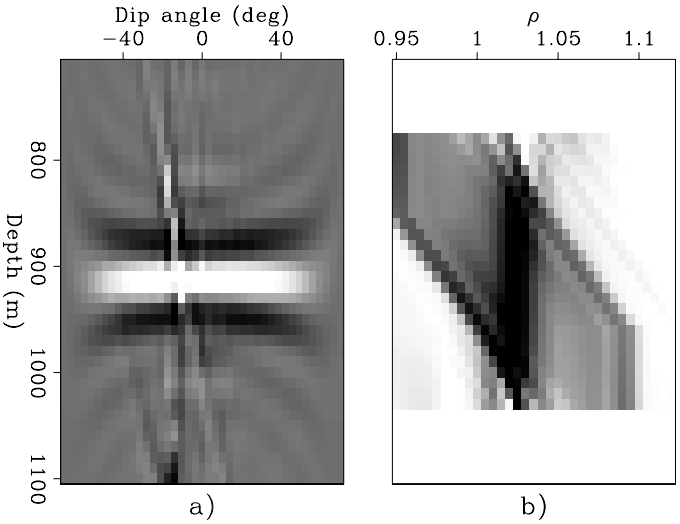

Figure 7: a) Dip-decomposed stack image of the diffractor-point window as a function of the dip angle extracted at $x = 4,700$ meters and $\rho = 1.025$), and (b) semblance ρ-spectrum computed at $x = 4,700$ meters. [**CR**]

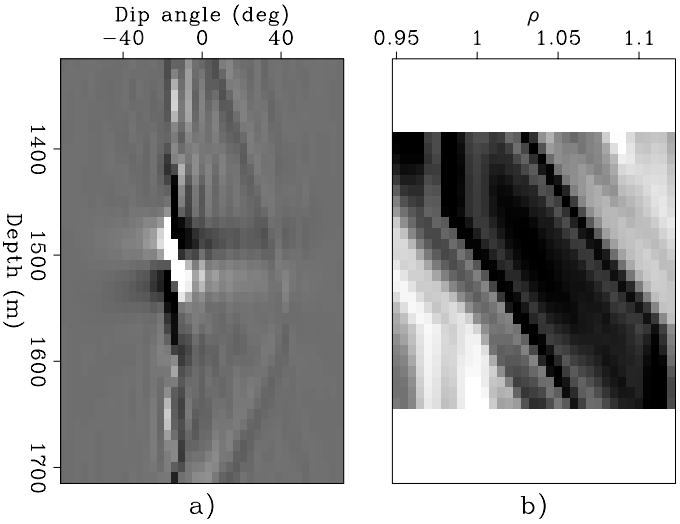

Figure 8: a) Dip-decomposed stack image of the reflector-truncation window as a function of the dip angle extracted at $x = 4,700$ meters and $\rho = 1.04$), and (b) semblance ρ-spectrum computed at $x = 4,700$ meters. [**CR**]

semblance functionals introduced in this paper, over spatial windows extending along both the z and x directions.

Figure 7a shows the dip-decomposed stack image of the diffractor-point window as a function of the dip angle α extracted from $\mathbf{R}(\mathbf{x}, \alpha, \rho)$ at the point-diffractor's horizontal position and for $\rho = 1.025$; that is, the correct value of ρ. The image is consistent as a function of dips, with the exception of an image artifact caused by interference with the image from the planar reflectors below the point diffractor. Figure 7b shows the semblance computed by applying equation 3 at the horizontal position of the point diffractor. It has a sharp peak for $\rho = 1.025$. The dip-coherency analysis has thus the potential to provide accurate velocity information.

Figure 8a shows the dip-decomposed stack image of the reflector-truncation window as a function of the dip angle α at extracted from $\mathbf{R}(\mathbf{x}, \alpha, \rho)$ at the horizontal position of the reflector's truncation for $\rho = 1.04$; that is, the correct value of ρ. The dip-decomposed image is strongly peaked at $\alpha = -15^o$; that is the dip of the reflector.

The event is weak away from $\alpha = -15^o$; and much weaker than the point-diffractor event shown in Figure 7a. Furthermore, polarity of the event switches at $\alpha = -15^o$. At the transition corresponding to the reflector dip, the image is actually rotated by 45 degrees. To compute a higher-quality semblance spectrum, I zeroed the image at $\alpha = -15^o$ and split the computation of the numerator in equation 3 between dips larger than 15 degrees and dips smaller than 15 degrees; that is I computed the following modified semblance functional:

$$S_{\bar{\alpha}}(\mathbf{x}, \rho) = \frac{\left[\sum_{\alpha<\bar{\alpha}} \sum_{\gamma} \mathbf{R}(\mathbf{x}, \gamma, \alpha, \rho)\right]^2 + \left[\sum_{\alpha>\bar{\alpha}} \sum_{\gamma} \mathbf{R}(\mathbf{x}, \gamma, \alpha, \rho)\right]^2}{(N_\alpha - 1) \sum_{\alpha\neq\bar{\alpha}} \left[\sum_{\gamma} \mathbf{R}(\mathbf{x}, \gamma, \alpha, \rho)\right]^2}, \tag{4}$$

where $\bar{\alpha}$ is the structural dip of the truncated reflector. The need to identify a reflector truncation and to estimate the local dip of the reflector is potentially a practical problem with using dip coherency to extract velocity information from reflector's truncations.

The semblance spectrum shown in Figure 8b was computed by applying equation 4 with $\bar{\alpha} = -15^o$. The semblance peak is at the correct value of $\rho = 1.04$ but it is much broader than the peak corresponding to the point diffractor shown in Figure 7b. As noted when comparing Figure 3a with Figure 4a, the velocity information provided by focusing analysis of reflectors' truncations seems to be more difficult to use than the one provided by point diffractors.

The computation of the dip spectra for the data set with sinusoidal reflector illustrates the limitations and potential dangers of relying on dip-only spectra when continuous reflectors have a strong curvature. Figures 9a and 9b show the image decomposed according to structural dips for the bottom of the syncline window for two different values of ρ: $\rho = .995$ for Figure 9a, and $\rho = 1.06$ for Figure 9b (same values of ρ as for Figure 5c and Figure 5b, respectively.) The image is flat as a function of the dip angle for the wrong value of ρ and is frowning for the correct value of ρ. Consequently the dip spectrum shown in Figure 9c peaks at a low value of ρ and would mislead velocity estimation.

The analysis of Figure 10 leads to similar conclusions. In this case the image is flat for a higher value of ρ ($\rho = 1.105$) than the correct one ($\rho = 1.045$), for which the image is actually smiling. The semblance spectrum is also biased toward higher values of ρ.

IMAGE-FOCUSING SEMBLANCE

In the previous section, I showed that we can measure image coherency across the structural dip axes to extract focusing information from stacked images. I also showed the shortcomings of this procedure in presence of reflector's curvature. In this section, I introduce a generalization of the semblance functional that measures coherency

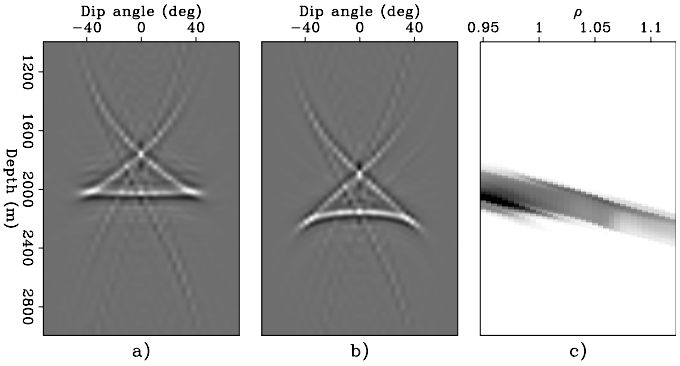

Figure 9: a) Dip-decomposed stack image of the bottom of the syncline window as a function of the dip angle extracted at $x = 4,250$ meters and $\rho = .995$), (b) dip-decomposed stack image for $\rho = 1.06$), and (c) semblance ρ-spectrum computed at $x = 4,250$ meters. [**CR**]

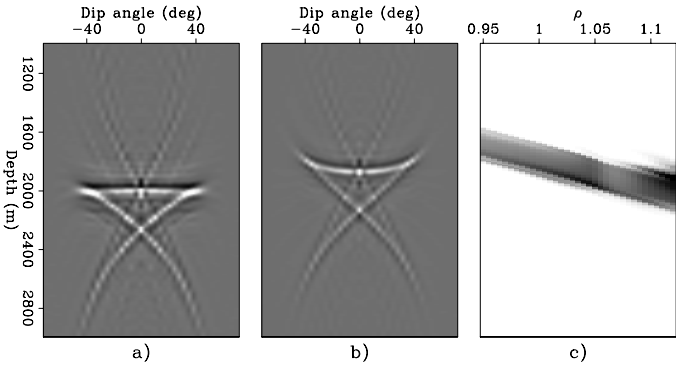

Figure 10: a) Dip-decomposed stack image of the top of the anticline window as a function of the dip angle extracted at $x = 4,750$ meters and $\rho = 1.105$), (b) dip-decomposed stack image for $\rho = 1.045$), and (c) semblance ρ-spectrum computed at $x = 4,750$ meters. [**CR**]

simultaneously along the dip axes and the aperture/azimuth axes. I name this semblance functional the *Image-focusing semblance*. In 2D it is defined as:

$$S_{(\gamma,\alpha)}(\mathbf{x},\rho) = \frac{\left[\sum_\gamma \sum_\alpha \mathbf{R}(\mathbf{x},\gamma,\alpha,\rho)\right]^2}{N_\gamma N_\alpha \sum_\gamma \sum_\alpha \mathbf{R}(\mathbf{x},\gamma,\alpha,\rho)^2}, \tag{5}$$

where N_γ is the number of aperture angles to be included in the computation.

As discussed in the previous section, the polarity of reflectors' truncation reverses at the reflectors' dip (Figure 8.) The semblance functional introduced in equation 5 can be modified to better measure image focusing of reflectors' truncation in a way analogous to the way I modified equation 3 to become equation 4. For reflector truncations, the image-focusing semblance can thus be computed as:

$$S_{(\gamma,\bar{\alpha})}(\mathbf{x},\rho) = \frac{\left[\sum_\gamma \sum_{\alpha<\bar{\alpha}} \mathbf{R}(\mathbf{x},\gamma,\alpha,\rho)\right]^2 + \left[\sum_\gamma \sum_{\alpha>\bar{\alpha}} \mathbf{R}(\mathbf{x},\gamma,\alpha,\rho)\right]^2}{N_\gamma (N_\alpha - 1) \sum_\gamma \sum_{\alpha\neq\bar{\alpha}} \mathbf{R}(\mathbf{x},\gamma,\alpha,\rho)^2}. \tag{6}$$

To better evaluate the amount of additional information provided by measuring coherency along the structural dips, I also computed a conventional semblance functional that measured coherency only along the aperture angle from the residual prestack migration results. I computed this conventional semblance function accord-

ing to the following expression:

$$S_\gamma\left(\mathbf{x},\rho\right)=\frac{\left[\sum_\gamma \mathbf{R}\left(\mathbf{x},\gamma,\rho\right)\right]^2}{N_\gamma \sum_\gamma \mathbf{R}\left(\mathbf{x},\gamma,\rho\right)^2}. \tag{7}$$

The ρ spectrum shown in Figure 11a was computed by applying equation 7. To compute the ρ spectrum shown in Figure 11b I used a combination of the semblance functional expressed in equation 5 for the two shallower events, and of the semblance functional expressed in equation 6 for the deepest event, which corresponds to the reflector's truncation. The semblance peak corresponding to the point diffractor (the top event) is much sharper in Figure 11b than in Figure 11a. This result confirms that the use of image-focusing semblance instead of conventional semblance has the potential of enhancing velocity estimation. In Figure 11b the semblance peaks corresponding to the planar dipping event (second from the top) and the reflector's truncation (first from the bottom) are substantially smaller than the one for the point diffractor, but are still located at the correct value of ρ. The relative scaling between the semblance peaks could be improved.

Figure 12 compares conventional aperture-angle ρ spectrum with the proposed image-focusing spectrum evaluated at the horizontal location of the bottom of the syncline in the model shown in Figure 2a. Both spectra peak for the correct value of ρ; that is $\rho = 1.06$. The spectrum computed using the proposed method has a small secondary peak for low ρs, but not as strong as the one for only-dip spectrum (Figure 9c) or the varimax norm (Figure 5a.) Similarly, the spectra computed at the horizontal location of the top of the anticline in the same model peak for the correct value of ρ, as shown in Figure 13.

CONCLUSIONS

Image-focusing analysis can provide useful velocity information, in particular in areas where conventional velocity analysis lacks resolution. Measuring image coherency across the structural-dip axes provides quantitative information on image focusing. However, in the presence of curved reflectors coherency across dips suffers similar shortcomings as conventional minimum entropy functional. To overcome these difficulties, I propose to perform image-focusing analysis by measuring image coherency simultaneously across structural dips and reflection aperture/azimuth angles. The application of the proposed image-focusing semblance to two synthetic data sets demonstrates its potential as a tool to extract quantitative velocity information from image-focusing analysis.

REFERENCES

Biondi, B., 2008, Automatic wave-equation migration velocity analysis: 2008, **134**, 65–77.

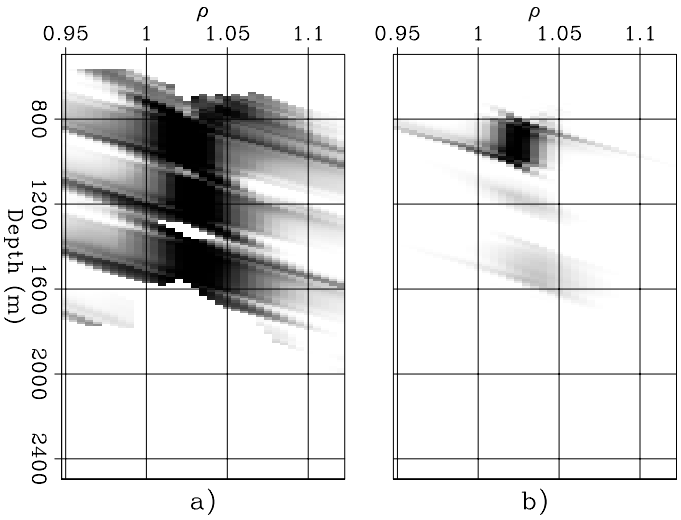

Figure 11: Semblance ρ spectra computed from the first data set (point diffractor and reflector truncations) at $x = 4,700$ meters with: (a) conventional aperture-angle semblance (equation 7,) and (b) aperture-angle and dip-angle semblance (equations 5 and 6.) [**CR**]

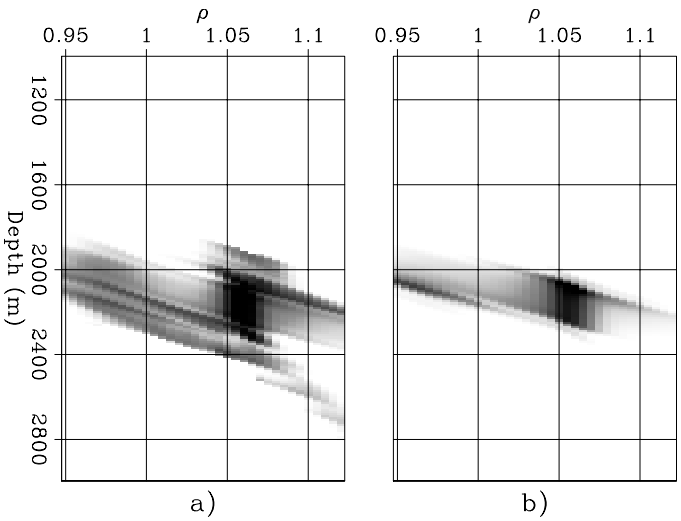

Figure 12: Semblance ρ spectra computed from the second data set (sinusoidal reflector) at $x = 4,250$ meters with: (a) conventional aperture-angle semblance (equation 7,) and (b) aperture-angle and dip-angle semblance (equation 5.) [**CR**]

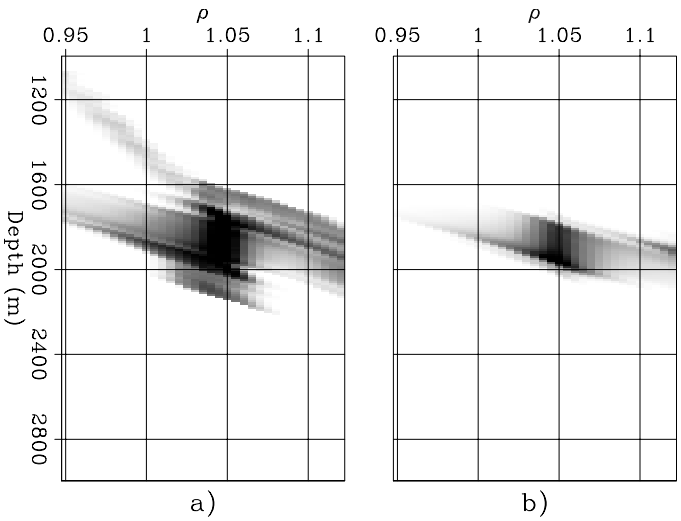

Figure 13: Semblance ρ spectra computed from the second data set (sinusoidal reflector) at $x = 4,750$ meters with: (a) conventional aperture-angle semblance (equation 7,) and (b) aperture-angle and dip-angle semblance (equation 5.) [**CR**]

Biondi, B. and P. Sava, 1999, Wave-equation migration velocity analysis: SEG Technical Program Expanded Abstracts, **18**, 1723–1726.

De Vries, D. and A. J. Berkhout, 1984, Velocity analysis based on minimum entropy: Geophysics, **49**, 2132–2142.

Fomel, S., E. Landa, and M. T. Taner, 2007, Poststack velocity analysis by separation and imaging of seismic diffractions: Geophysics, **72**, U89–U94.

Harlan, W. S., J. F. Claerbout, and F. Rocca, 1984, Signal/noise separation and velocity estimation: Geophysics, **49**, 1869–1880.

Sava, P., 2004, Migration and velocity analysis by wavefield extrapolation: PhD thesis, Stanford University.

Sava, P. and B. Biondi, 2004a, Wave-equation migration velocity analysis—I: Theory: Geophysical Prospecting, **52**, 593–623.

———, 2004b, Wave-equation migration velocity analysis—II: Examples: Geophysical Prospecting, **52**, 607–623.

Sava, P. C., 2003, Prestack residual migration in frequency domain: Geophysics, **68**, 634–640.

Sava, P. C., B. Biondi, and J. Etgen, 2005, Wave-equation migration velocity analysis by focusing diffractions and reflections: Geophysics, **70**, U19–U27.

Stinson, K., E. Crase, W.-K. Chan, and S. Levy, 2005, Optimized determination of migration velocities: Recorder, **30**, 5–6.

Wang, B., V. Dirks, P. Guillaume, F. Audebert, and D. Epili, 2006, A 3d subsalt tomography based on wave-equation migration-perturbation scans: Geophysics, **71**, E1–E6.

Wiggins, R., 1985, Entropy guided deconvolution: Geophysics, **50**, 2720–2726.